

Dynamics of a single ion spin impurity in a spin-polarized atomic bath

H. Fürst,¹ T. Feldker,¹ N. V. Ewald,¹ J. Joger,¹ M. Tomza,² and R. Gerritsma¹

¹*Van der Waals-Zeeman Institute, Institute of Physics, University of Amsterdam, 1098 XH Amsterdam, The Netherlands*

²*Faculty of Physics, University of Warsaw, Pasteura 5, 02-093 Warsaw, Poland*

(Dated: February 18, 2022)

We report on observations of spin dynamics in single Yb^+ ions immersed in a cold cloud of spin-polarized ^6Li atoms. This species combination has been proposed to be the most suitable system to reach the quantum regime in atom-ion experiments. For $^{174}\text{Yb}^+$, we find that the atomic bath polarizes the spin of the ion by 93(4) % after a few Langevin collisions, pointing to strong spin-exchange rates. For the hyperfine ground states of $^{171}\text{Yb}^+$, we also find strong rates towards spin polarization. However, relaxation towards the $F = 0$ ground state occurs after 7.7(1.5) Langevin collisions. We investigate spin impurity atoms as possible source of apparent spin-relaxation leading us to interpret the observed spin-relaxation rates as an upper limit. Using *ab initio* electronic structure and quantum scattering calculations, we explain the observed rates and analyze their implications for the possible observation of Feshbach resonances between atoms and ions once the quantum regime is reached.

I. INTRODUCTION

In recent years, a novel field of physics and chemistry has developed in which cold trapped ions and ultracold atomic gases are made to interact with each other [1–21]. These efforts were motivated by the prospect of attaining ultra-cold ions [22] by e.g. sympathetic cooling [16, 23–25] with atoms, probing atomic systems with ions [26] and proposals to use the system for quantum computation [27, 28] and quantum simulation [29]. However, these ideas require reaching ultra-cold temperatures to enter the quantum regime which has proven very hard. The main problem is posed by the time-dependent trapping field of the Paul trap used to confine the ions. During a collision between an atom and an ion, energy can be transferred from this field to the system, limiting attainable temperatures [3, 4, 16, 24, 30–35]. In reference [31], it was calculated that the lowest temperatures may be reached for the largest ion/atom mass ratios m_i/m_a . In this work, we employ the ion/atom combination with the highest mass ratio of all species that allow for straightforward laser cooling, $m_i/m_a \approx 24$ –29 given by Yb^+/Li . For this combination, the quantum (or *s*-wave) regime is attained at a collision energy of $k_B \cdot 8.6 \mu\text{K}$, which should be in reach in state-of-the-art setups [35].

For ion-atom mixtures to be used in quantum technology applications - in which quantum information will be stored in the internal states of the ions and atoms - it is required that spin-changing collision rates are small [36]. In a recent experiment Ratschbacher *et al.* [14] showed very fast spin dynamics in Yb^+ interacting with Rb atoms. Besides fast spin exchange - which conserves the total spin of the collision partners - strong spin-nonconserving rates known as spin-relaxation were observed. Very recently, spin-dynamics were also measured in Sr^+/Rb [19]. Tscherbul *et al.* [37] calculated that an exceptionally large second-order spin-orbit coupling in Yb^+/Rb provides a mechanism for the observed spin-relaxation rates. For Yb^+/Li the second-order spin-orbit coupling is expected to be much smaller [37]. A detailed

knowledge about the spin-dependence in cold atom-ion collisions gives insight into the possibilities of finding magneto-molecular (Feshbach) resonances between the atoms and ions [38–41]. These play a pivotal role in neutral atomic systems for tuning the atom-atom interactions and find widespread application in studying atomic quantum many-body systems [38, 42]. In ion-atom mixtures, their existence has been predicted [39, 40], but they have not been observed so far since the required low temperatures have not been reached. These considerations make an experimental study of the spin-dynamics in Yb^+/Li of key interest.

In this work, we investigate the spin dynamics of single trapped Yb^+ ions in a cold, spin-polarized bath of ^6Li atoms. We prepare specific (pseudo-) spin states in the ion by optical pumping and microwave pulses. Electron shelving and fluorescence detection allow us to determine the spin state after interacting with the atomic cloud.

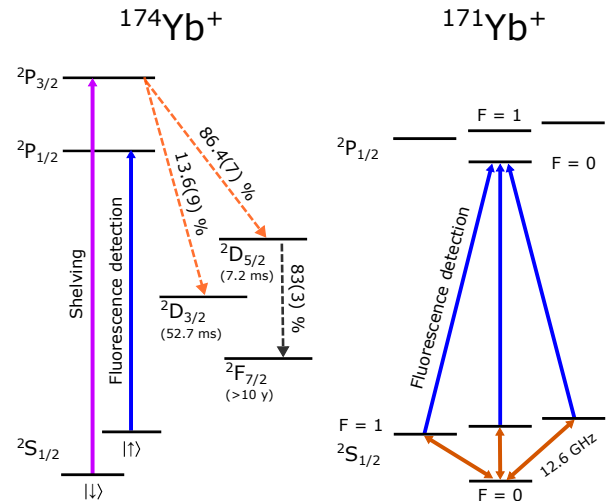


FIG. 1. Energy levels and relevant transitions in $^{174}\text{Yb}^+$ and $^{171}\text{Yb}^+$.

For $^{174}\text{Yb}^+$ we find that the cloud of atoms polarizes the spin of the ion by 93(4)%. Our results indicate a very large spin-exchange rate of $1.03(12) \cdot \gamma_L$, whereas spin-relaxation rates are estimated to be $\leq 0.08(4) \cdot \gamma_L$. Here, $\gamma_L = 2\pi\rho_{\text{Li}}\sqrt{C_4/\mu} = 22(7) \text{ s}^{-1}$ is the Langevin collision rate, with ρ_{Li} the density of Li atoms at the location of the ion, C_4 is proportional to the polarizability of the atom and μ is the reduced mass. For the $^{171}\text{Yb}^+$ isotope, we prepare all four hyperfine ground states and measure all decay rates. As in $^{174}\text{Yb}^+$, we find strong rates towards spin polarization. However, relaxation from the $m_F = 1$ state towards the $F = 0$ ground state occurs at a rate of $0.13(3) \cdot \gamma_L$. All relevant energy levels of both Yb^+ isotopes can be seen in Fig. 1. We combine *ab initio* quantum scattering calculations with the measured spin dynamics. Interestingly, we find in our calculations that even in the mK temperature regime the spin-exchange rates still depend strongly on the difference between assumed singlet (a_S) and triplet (a_T) scattering lengths. A similar effect was observed in [43, 44]. Our results indicate a large difference between the singlet and triplet scattering lengths in Yb^+/Li , which will be beneficial for the observation of Feshbach resonances. Our electronic structure calculations also confirm that spin-nonconserving relaxation rates due to second-order spin-orbit coupling should be smaller than for Yb^+/Rb [37].

II. EXPERIMENT

A. Setup

The experimental setup has been described in detail in Ref. [45]. In short, a cloud of magnetically trapped ^6Li atoms in the $^2S_{1/2} |F = 3/2, m_F = 3/2\rangle$ electronic ground state is prepared 2.1 cm below the ion. The atoms are transported towards the ion by adiabatically changing the magnetic field minimum position to a position $150 \mu\text{m}$ below the ion, where the $\sim 400 \mu\text{m}$ wide cloud interacts with the ion for a period of time t_{int} . Afterwards, the atoms are transported back, released from the trap and imaged on a CCD camera. Approximately $7 \cdot 10^6$ atoms interact with the trapped ion at a peak density of $49(15) \cdot 10^{14} \text{ m}^{-3}$ and a temperature of $T_a = 0.6(2) \text{ mK}$.

The energy of the ion is composed of its micromotion in the Paul trap and its secular energy. Before the experiment, we measured and compensated the ion's excess micromotion in all three dimensions as described in Ref. [45]. We estimate a residual excess micromotion energy of $\approx 2 \text{ mK}$ per direction. We employ microwave sideband spectroscopy on a single $^{171}\text{Yb}^+$ ion [46, 47] and infer an ion temperature in the secular motion of $\approx 4 \text{ mK}$ after Doppler cooling and a heating rate of less than 4 mK/s . The combined energy of the ion is $E_{\text{Yb}}/k_B \leq 20 \text{ mK}$ during the experiments. Due to the large mass ratio m_i/m_a , however, the collision energy $E_{\text{col}} = \frac{\mu}{m_{\text{Yb}}} E_{\text{Yb}} + \frac{\mu}{m_{\text{Li}}} E_{\text{Li}} \approx k_B \cdot 1 \text{ mK}$ is dominated by the energy of the atoms.

During the interaction, the ion experiences a magnetic field of 0.42 mT caused by the magnetic trap. The energy splitting of the ion's magnetic sublevels is therefore kept small, allowing for spin-exchange. Following each experimental run, control measurements are performed to verify the conservation of the ionic spin in the sequence when no atoms are loaded.

B. Spin preparation and detection

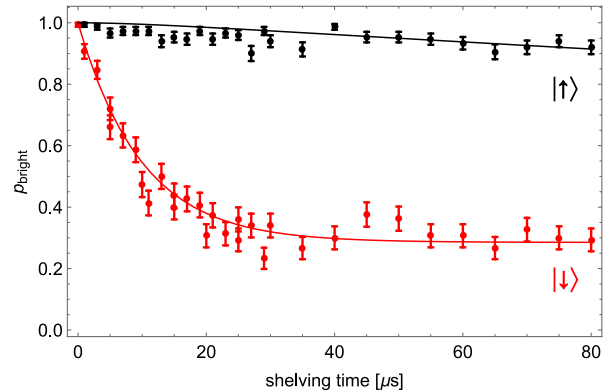


FIG. 2. Probability for finding an ion in the bright state versus duration of the 329 nm shelving pulse. When initially prepared in the $|\downarrow\rangle$ state (red/grayscale) the ion remains unshelved with a probability of 28(3)%, whereas in the case of $|\uparrow\rangle$ (black) the ion is only shelved off-resonantly. The data is shown along with an analytic model that involves all relevant levels.

To initialize the $^{174}\text{Yb}^+$ ion in a Zeeman level of the $^2S_{1/2}$ ground state, we apply a pulse of resonant circularly polarized light on the 369 nm cooling transition along the trap axis. A small magnetic bias field pointing either parallel or anti-parallel along the trap axis is used to prepare each of the two Zeeman states. We measure the optical pumping efficiency by comparing the fluorescence during the optical pumping pulses for the correct σ -polarization and the fluorescence for linear polarization with the case where no ion is present. From these measurements we obtain an optical pumping efficiency of 98.5(6)% for the $|^2S_{1/2}, m_J = 1/2\rangle = |\uparrow\rangle$ state and 97.8(7)% for the $|^2S_{1/2}, m_J = -1/2\rangle = |\downarrow\rangle$ state.

To detect the spin state after the interaction with the cloud of atoms, we state-selectively shelve the ion into the long-lived $^2F_{7/2}$ state as sketched in Fig. 1 (left). We therefore apply a homogeneous magnetic field of 72.5 mT to separate the $^2S_{1/2} \rightarrow ^2P_{3/2}$ transitions by 680 MHz and irradiate a shelving pulse resonant with the $|\downarrow\rangle \rightarrow |^2P_{3/2}, m_J = -3/2\rangle$ transition, allowing for a decay channel via $^2D_{5/2}$ to the $^2F_{7/2}$ state with a probability of 72(3)% [48–50]. We measure the probability for finding the ion being still in the $^2S_{1/2}$ ground state by switching off the magnetic field after the shelving and subsequent detection of the fluorescence during Doppler

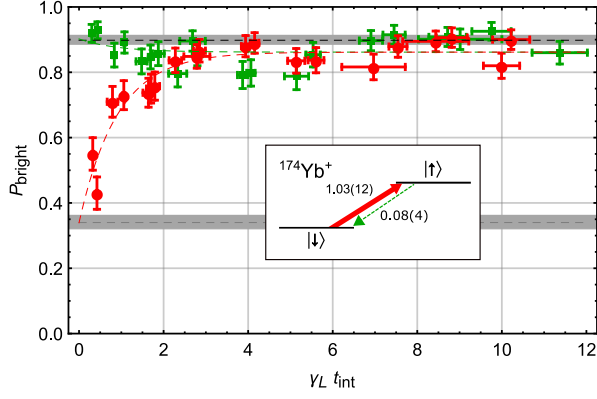


FIG. 3. Probability for finding the $^{174}\text{Yb}^+$ ion in the bright state versus interaction time in units of the inverse Langevin rate. The gray bars indicate the minimum (for $|\downarrow\rangle$) and maximum (for $|\uparrow\rangle$) probabilities to find the ion in a bright state and their error range when no atoms are loaded, indicating the limits of the employed preparation and shelving techniques. The dashed lines are obtained from a combined two-level rate equation fit (Eq. 1). The inset shows the obtained spin flip rates of the two Zeeman sublevels in units of Langevin rates.

cooling. The remaining population in the $^2S_{1/2}$ state then contains both the unshelved and the imperfectly shelved Zeeman state. After state detection we depopulate the metastable $^2F_{7/2}$ state using a pulse of 638 nm light to re-enter the cooling cycle.

The resulting probabilities to find the population unshelved as a function of shelving pulse length is shown in Fig. 2 for the ion being initially prepared in either $|\downarrow\rangle$ (red) or $|\uparrow\rangle$ (black). We model the data using a rate equation that involves all relevant levels and a saturation parameter of $s = 0.12$, matching our observations. We obtain a probability of 9(1)% for the $|\uparrow\rangle$ state to be off-resonantly shelved after 80 μs of shelving light. If the ion is prepared in the $|\downarrow\rangle$ state, we find a probability of 28(3)% to remain unshelved.

To study the dynamics of the $^{171}\text{Yb}^+$ hyperfine states, we initialize the ion in $F = 0$ via optical pumping [51] and apply a microwave pulse (rapid adiabatic passage) to prepare one of the three $F = 1$ sublevels before the interaction with the atoms. After the interaction, we measure the population in the $F = 1$ state by state-selective fluorescence imaging to obtain a signal proportional to $\sum_{m_F} p_{|1,m_F\rangle} = 1 - p_{|0,0\rangle}$ as depicted in Fig. 1 (right). To analyze the population in each of the magnetic sublevels, we invert $p_{|1,m_F\rangle}$ with $p_{|0,0\rangle}$ by applying a second microwave pulse before detection to get a signal proportional to $1 - p_{|1,m_F\rangle}$.

III. RESULTS

A. $^{174}\text{Yb}^+$

We scan the atom-ion interaction time t_{int} in units of the inverse Langevin rate $1/\gamma_L$ for $^{174}\text{Yb}^+$ initially prepared in one of the two spin states. The results are shown in Fig. 3. When the ion is initialized in $|\downarrow\rangle$ (red discs), around one Langevin collision is sufficient to flip its spin. In contrast, when initialized in the $|\uparrow\rangle$ state (green squares), the ion keeps its initial polarization. We fit the data to a two-level rate equation model [14],

$$\begin{aligned} P_{b,\uparrow}(t_{\text{int}}) &= (P_{b,\uparrow}^0 - P_b^\infty) e^{-\gamma_{\text{eq}} t_{\text{int}}} + P_b^\infty, \\ P_{b,\downarrow}(t_{\text{int}}) &= (P_b^\infty - P_{b,\downarrow}^0) (1 - e^{-\gamma_{\text{eq}} t_{\text{int}}}) + P_{b,\downarrow}^0, \end{aligned} \quad (1)$$

where P_{b,m_J}^0 are the probabilities to find an ion prepared in $|m_J\rangle$ to be in the bright state when no atoms were loaded (lower and upper gray bars in the plot), resembling the limits of our optical pumping and shelving technique. P_b^∞ is the equilibrium probability to appear bright after interaction with the atomic cloud. For the equilibration rate we obtain $\gamma_{\text{eq}} = 1.1(1) \cdot \gamma_L$. In the two-level model $\gamma_{\text{eq}} = \gamma_+ + \gamma_-$, with γ_\pm the rates for $\Delta m_J = \pm 1$ transitions of the Zeeman state respectively. From the control measurements (without atoms) we get $P_{b,\downarrow}^0 = 0.34(2)$ and $P_{b,\uparrow}^0 = 0.90(2)$. Together with the equilibrium probability $P_b^\infty = 0.86(1)$ we obtain the equilibrium polarization of the ion $p_\uparrow^\infty = (P_b^\infty - P_{b,\downarrow}^0)/(P_{b,\uparrow}^0 - P_{b,\downarrow}^0) = 0.93(4)$ as well as $\gamma_+ = 1.03(12) \cdot \gamma_L$ and $\gamma_- = 0.08(4) \cdot \gamma_L$ from the relation $p_\uparrow^\infty = \gamma_+ / (\gamma_+ + \gamma_-)$.

B. $^{171}\text{Yb}^+$

The data obtained in the determination of population in the hyperfine states of $^{171}\text{Yb}^+$ was fitted by the solutions of the four-level coupled rate equations

$$\begin{bmatrix} \dot{p}_{|0,0\rangle} \\ \dot{p}_{|1,-1\rangle} \\ \dot{p}_{|1,0\rangle} \\ \dot{p}_{|1,1\rangle} \end{bmatrix} = \hat{D} \begin{bmatrix} p_{|0,0\rangle} \\ p_{|1,-1\rangle} \\ p_{|1,0\rangle} \\ p_{|1,1\rangle} \end{bmatrix}, \quad (2)$$

with the dot denoting the time derivative and the decay matrix

$$\hat{D} = \begin{bmatrix} 0 & \Gamma_{-1} & \Gamma_0 & \Gamma_1 \\ 0 & -\Gamma_{-1} - \gamma_{-1,0} & \gamma_{0,-1} & 0 \\ 0 & \gamma_{-1,0} & -\Gamma_0 - \gamma_{0,1} - \gamma_{0,-1} & \gamma_{1,0} \\ 0 & 0 & \gamma_{0,1} & -\Gamma_1 - \gamma_{1,0} \end{bmatrix},$$

where Γ_{m_F} denote the rates from $|1, m_F\rangle$ to $|0, 0\rangle$ and γ_{m_F, m'_F} denote the rates from $|1, m_F\rangle$ to $|1, m'_F\rangle$. Note that we assumed the $\Delta m_F = \pm 2$ rates to be zero and that transitions changing the total angular momentum by $\Delta F = +1$ are energetically forbidden due to the 12.6 GHz

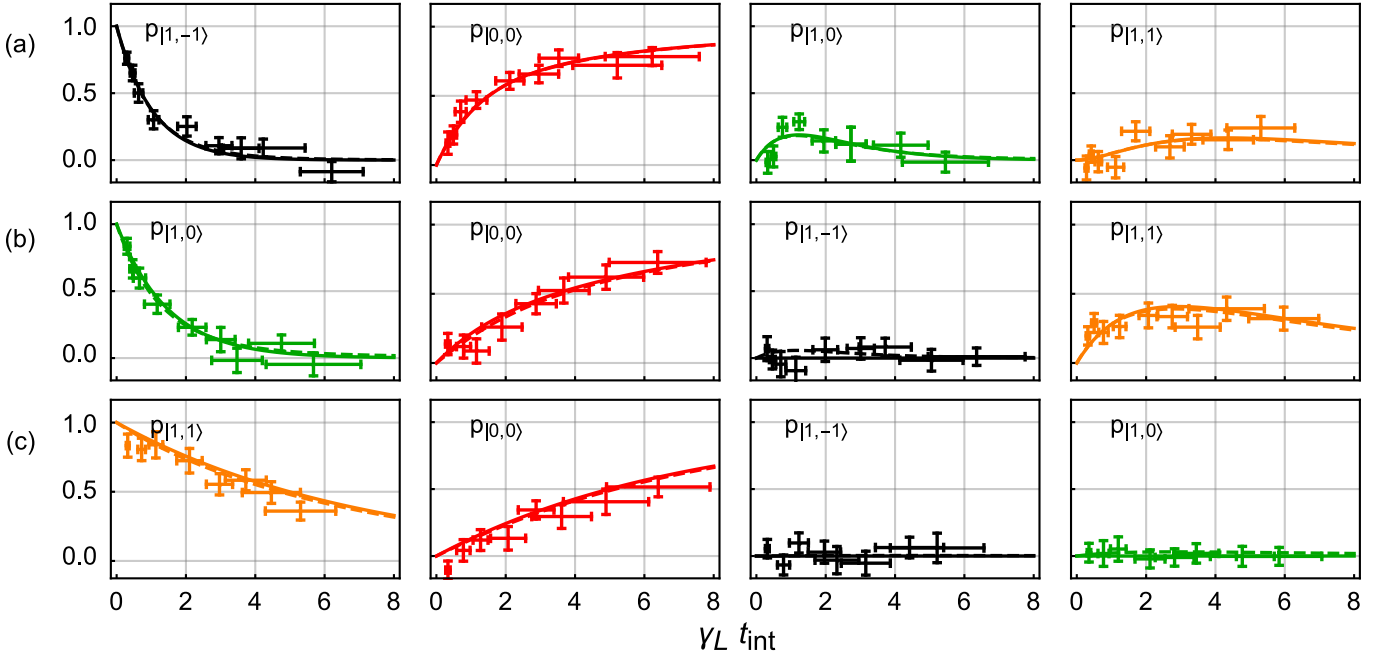


FIG. 4. Collision-induced population transfer in the $^{171}\text{Yb}^+$ hyperfine ground state after the preparation of $|1, -1\rangle$ (row (a)), $|1, 0\rangle$ (row (b)) and $|1, 1\rangle$ (row (c)). The first column shows the decay of the initially prepared state in the $F = 1$ manifold and the second column the build up of population in the $F = 0$ ground state. The other two columns show the population dynamics of two other states in $F = 1$. The lines are obtained from a combined fit model assuming the rates for $\Delta m_F = -1$ within the $F = 1$ manifold to be zero (solid) or allowing for all decay channels (dashed). The interaction time is given in units of the inverse Langevin rate.

hyperfine splitting. To obtain analytic solutions of Eq. 2, we need to set the spin-nonconserving $\Delta m_F = -1$ rates $\gamma_{0,-1}$ and $\gamma_{1,0}$ to be zero, since there was no clear evidence for these events in the experimental data, as shown in the twelve relevant plots in Fig. 4. To obtain upper bounds on these two rates, we take the fitted curves (solid lines) as an initial guess and numerically minimize the mean quadratic distance of the full numerical solutions of Eq. 2 to the experimental data. The optimized solutions are shown as dashed lines and deviate only slightly from the initial guess.

The resulting rates are shown in Fig. 5. While the transition rates γ_{m_F, m'_F} for $\Delta m_F = m'_F - m_F = +1$ within the $F = 1$ manifold are both approximately equal to $\gamma_{-1,0} = 0.44(11) \cdot \gamma_L \approx \gamma_{0,1} = 0.44(8) \cdot \gamma_L$, the rates Γ_{m_F} changing the total angular momentum by $\Delta F = -1$ decrease with increasing m_F in the $F = 1$ manifold from $\Gamma_{-1} = 0.57(8) \cdot \gamma_L$ via $\Gamma_0 = 0.21(7) \cdot \gamma_L$ to $\Gamma_1 = 0.13(3) \cdot \gamma_L$. Note that the decay Γ_1 does not conserve the total spin of the atom-ion system. The rates changing only m_F by -1 are hardly detectable in our experiment due to the dominating rates Γ_0 and Γ_{-1} .

C. Purity of atomic spin

The observed spin-nonconserving rates γ_- and Γ_1 could be due to second-order spin-orbit coupling that

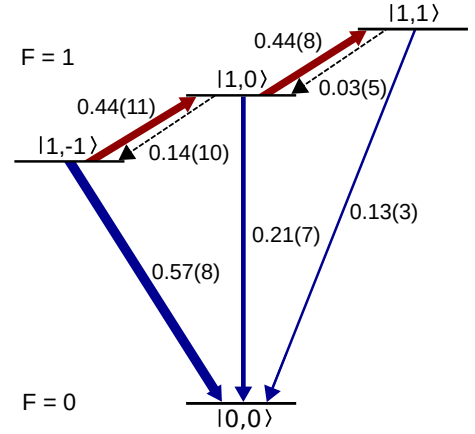


FIG. 5. Measured transition rates between the $^{171}\text{Yb}^+ \ ^2\text{S}_{1/2}$ hyperfine ground states in units of the Langevin rate γ_L . The $\Delta m_F = +1$ processes (dark red, pointing up right) dominate the dynamics, whereas the $\Delta m_F = -1$ transitions (dashed, black) can hardly be detected. The $\Delta F = -1$ transitions are shown in blue (pointing towards $F = 0$).

was recently suggested as a source of spin-relaxation [37]. However, another possibility is that atomic spin impurities within the gas cause sporadic collisions that appear as spin non-conserving. In particular, we ex-

pect the presence of atoms in the low-field seeking $|3/2, 1/2\rangle$ state due to imperfect optical pumping. When such impurity atoms collide with a spin-polarized ion, spin-allowed transitions such as $|3/2, 1/2\rangle_{\text{atom}} |1, 1\rangle_{\text{ion}} \rightarrow |3/2, 3/2\rangle_{\text{atom}} |0, 0\rangle_{\text{ion}}$ may occur that cannot be distinguished from spin-relaxation caused by majority atoms. In this subsection, we study the spin purity of the atomic cloud.

The spin of the atoms in the magnetic trap is polarized by applying a $150\text{ }\mu\text{s}$ σ^+ -polarized optical pumping pulse at the D1 transition while applying an additional magnetic field of 1.0 mT along the beam direction. Due to magnetic field inhomogeneities not every atom is in the correct magnetic field to be pumped resonantly to the desired $|F = 3/2, m_F = 3/2\rangle$ ground state. To estimate the purity of the magnetically trapped ^6Li cloud in the $|3/2, 3/2\rangle$ state, we perform a Stern-Gerlach experiment. We abruptly displace the trap minimum radially by approximately 6 mm in less than a millisecond while keeping the gradient constant at $g_r = 0.22\text{ T/m}$. To image the accelerating cloud, we switch off the trapping field after a variable time t_{SG} . We wait 1 ms for the magnetic fields to settle and take an absorption image. After $t_{\text{SG}} = 11.5\text{ ms}$ the atoms in the $|3/2, 1/2\rangle$ state have separated from the main fraction in the $|3/2, 3/2\rangle$ state caused by the difference in magnetic moment, in agreement with simulations. To make sure we image both fractions equally well, we scanned the imaging laser frequency $\pm 10\text{ MHz}$ around the resonance and average over the results. In order to obtain the fraction of $|3/2, 1/2\rangle$ atoms, we project the images along the vertical axes, as it is shown in Fig. 6. The atoms in the $|3/2, 1/2\rangle$ state (left peak) did not pass the trap minimum at around

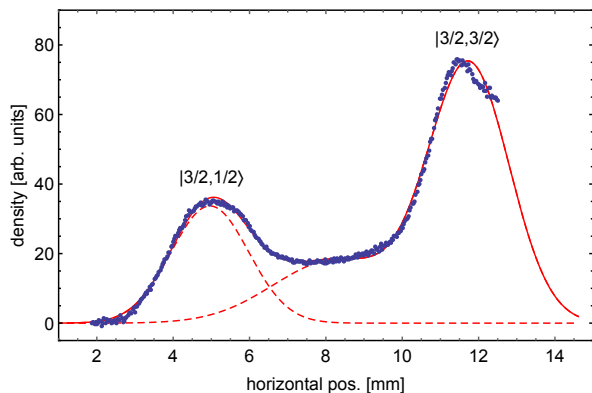


FIG. 6. Projected absorption image for a Stern-Gerlach acceleration time of $t_{\text{SG}} = 11.5\text{ ms}$ (blue points). The smaller peak on the left corresponds to the signal of the impurity atoms in the undesired $|3/2, 1/2\rangle$ state lagging behind the atoms in $|3/2, 3/2\rangle$ (right). Note that the x-axis points in the direction of acceleration. The data was fit using the sum of three Gaussian distributions (red, solid), one for the impurity atoms (dashed, left) and two to model the majority atoms and the tail in between (dashed, right).

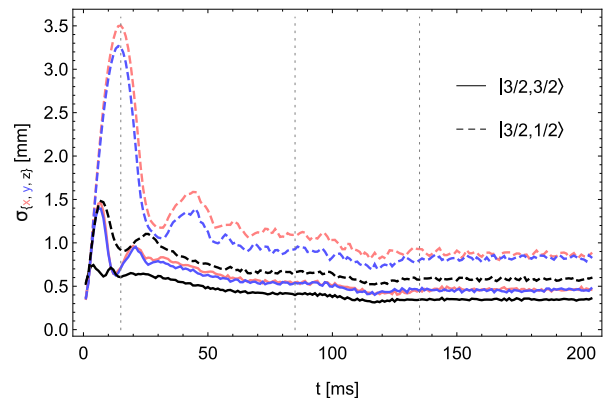


FIG. 7. Simulated evolution of the horizontal (x , light red/gray, y , blue/dark gray) and vertical (z , black) cloud sizes of $|3/2, 3/2\rangle$ (solid) and $|3/2, 1/2\rangle$ (dashed) for loading the magnetic trap from a compressed MOT (0-15 ms) followed by a compressing transport to the interaction zone (the cloud is moved in the x -direction during the time-interval 15-85 ms, and in the z -direction during the time-interval 85-135 ms). For more details, see Ref. [45].

6 mm yet whereas the atoms in the $|3/2, 3/2\rangle$ state have reached their turning point at around 12 mm and show a long tail lagging behind, in agreement with simulations. Due to the lack of a suitable model, we fit the data with the sum of three Gaussian distributions (red, solid), one for the $|3/2, 1/2\rangle$ state and two for the $|3/2, 3/2\rangle$ state to model the tail of the distribution (red, dashed). By comparing the peak integrals, we obtain a fraction of $\tilde{N}_{|3/2, 1/2\rangle} = N_{|3/2, 1/2\rangle}/N_{\text{tot}} = 24(1)\%$ of the atoms being in the undesired state.

Due to the difference in magnetic moment, the spatial distribution for the $|3/2, 1/2\rangle$ state is expected to be broader than for the $|3/2, 3/2\rangle$ state. Thus the possibility to find an impurity atom at the ion's position, given by $\tilde{\rho}_{|3/2, 1/2\rangle} = \rho_{|3/2, 1/2\rangle}/\rho_{\text{tot}}$, is reduced with respect to the fraction $\tilde{N}_{|3/2, 1/2\rangle}$. To estimate this ratio, we assume both fractions of the cloud to have the same initial size and temperature before they are loaded into the magnetic trap, justified by their origin from a compressed magneto-optical trap (cMOT). When transferring the atoms from the cMOT to the magnetic trap both temperature and size of the clouds change, depending on their magnetic moment, proportional to their m_F quantum number at low magnetic fields. Using realistic parameters obtained from the experiment, we simulate this transfer to the magnetic trap followed by a combined compression and transport to the interaction zone within 135 ms . The temporal evolution of the cloud sizes is shown in Fig. 7. While the cloud size in $|3/2, 3/2\rangle$ remains almost unchanged, the impurity fraction initially expands because of its weaker trapping potential. Thus we obtain a fractional density of $\tilde{\rho}_{|3/2, 1/2\rangle} \leq 10\%$ at the position of the ion. Due to the increased cloud size, we assume to lose a large fraction of the impurity atoms during the magnetic

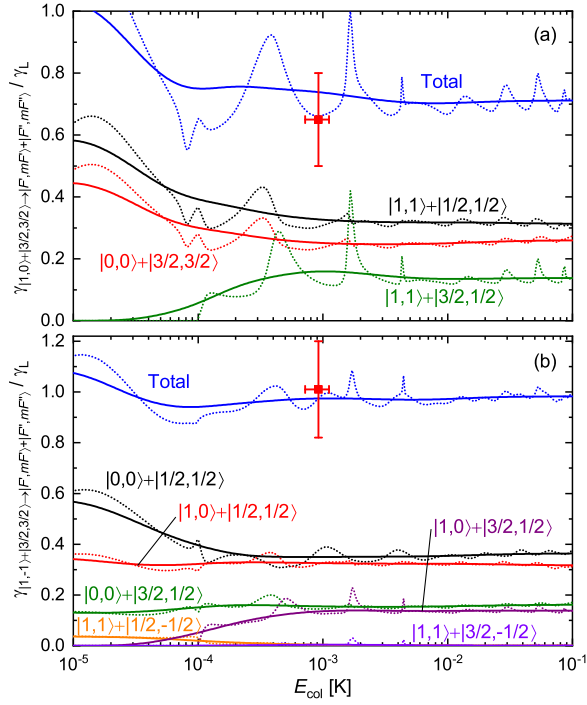


FIG. 8. Total spin-exchange rates and their decompositions onto all possible spin states for $^{171}\text{Yb}^+/\text{}^6\text{Li}$ versus collision energy obtained in coupled-channel scattering calculations compared with measured rates. Panel (a) for the $|1,0\rangle$ state and (b) for the $|1,-1\rangle$ state of the $^{171}\text{Yb}^+$ ion. Triplet and singlet scattering lengths of $a_T = -a_S = R_4$ are assumed. Dotted lines are energy-resolved rates and solid lines are thermally averaged rates.

transport by collisions with the ion trap electrodes such that the actual density fraction is expected to be lower than in the simulation. Furthermore, spin-exchange with majority atoms occurs, leading to the loss of the impurity atoms [52]. We justify these assumptions by performing the same Stern-Gerlach experiment as described above, but on the atoms that return after the interaction time, where we cannot observe an impurity spin signal anymore. However, since we cannot rule out the presence of some impurity atoms at the location of the ion, we treat the measured spin-nonconserving rates γ_- and Γ_1 as an upper limit.

IV. THEORY

To explain the measured rates, we construct and solve a quantum microscopic model of cold atom-ion interactions and collisions based on the *ab initio* coupled-channel description of the Yb^+/Li system we developed in Ref. [40]. As an entrance channel, we assume Li in a spin-polarized state and Yb^+ in a selected state, while all allowed exit channels are included in the model.

A. Spin exchange rates

To explain the observed spin-exchange rates, we perform *ab initio* quantum scattering calculations as implemented in Refs. [40, 53]. The Hamiltonian describing the nuclear motion of the Yb^+/Li atom-ion system reads

$$\hat{H} = -\frac{\hbar^2}{2\mu} \frac{1}{R} \frac{d^2}{dR^2} R + \frac{\hat{l}^2}{2\mu R^2} + \sum_{S, M_S} V_S(R) |S, M_S\rangle \langle S, M_S| + \hat{H}_{\text{dip}} + \hat{H}_{\text{Yb}^+} + \hat{H}_{\text{Li}}, \quad (3)$$

where R is the atom-ion distance, \hat{l} is the rotational angular momentum operator, μ is the reduced mass, and $V_S(R)$ is the potential energy curve for the state with total electronic spin S . \hat{H}_{dip} is the effective dipolar-like interaction. The atomic Hamiltonian, \hat{H}_j ($j = \text{Yb}^+, \text{Li}$), including hyperfine and Zeeman interactions, is given by

$$\hat{H}_j = \zeta_j \hat{i}_j \cdot \hat{s}_j + \left(g_e \mu_B \hat{s}_{j,z} + g_j \mu_N \hat{i}_{j,z} \right) B_z, \quad (4)$$

where \hat{s}_j and \hat{i}_j are the electron and nuclear spin operators, ζ_j is the hyperfine coupling constant, $g_{e/j}$ is the electron/nuclear g factor, and $\mu_{B/N}$ is the Bohr/nuclear magneton, respectively. For the fermionic $^{171}\text{Yb}^+$ ion, Eq. (4) reduces to the electronic Zeeman term. A magnetic field of 0.42 mT is assumed in all calculations, as used in the experiment.

We use potential energy curves for the $a^3\Sigma^+$ and $A^1\Sigma^+$ electronic states as calculated in Ref. [40]. The scattering lengths are fixed by applying uniform scaling factors λ_S to the interaction potentials: $V_S(R) \rightarrow \lambda_S V_S(R)$. We express scattering lengths in units of the characteristic length scale for the ion-atom interaction $R_4 = \sqrt{2\mu C_4/\hbar}$.

We construct the total scattering wave function in a fully uncoupled basis set,

$$|i_{\text{Yb}^+}, m_{i,\text{Yb}^+}\rangle |s_{\text{Yb}^+}, m_{s,\text{Yb}^+}\rangle |i_{\text{Li}}, m_{i,\text{Li}}\rangle |s_{\text{Li}}, m_{s,\text{Li}}\rangle |l, m_l\rangle,$$

where m_j is the projection of angular momentum j on the space-fixed z -axis, assuming the projection of the total angular momentum $M_{\text{tot}} = m_{f,\text{Yb}^+} + m_{f,\text{Li}} + m_l = m_{i,\text{Yb}^+} + m_{s,\text{Yb}^+} + m_{i,\text{Li}} + m_{s,\text{Li}} + m_l$ to be conserved. We solve the coupled-channels equations using a renormalized Numerov propagator [54] with step-size doubling and about 100 step points per de Broglie wavelength. The wave function ratio Ψ_{i+1}/Ψ_i at the i -th grid step is propagated to large interatomic separations, transformed to the diagonal basis, and the K and S matrices are extracted by imposing long-range scattering boundary conditions in terms of Bessel functions.

We calculate elastic $K_{\text{el}}^i(E)$ and inelastic $K_{\text{in}}^i(E)$ rate constants for collisions in the i -th channel from the diagonal elements of the S matrix summed over partial

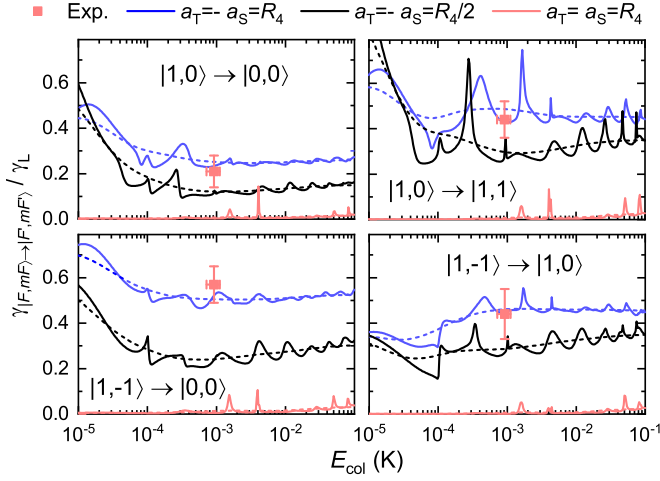


FIG. 9. Spin-exchange transition rates for $^{171}\text{Yb}^+$ versus collision energy obtained in coupled-channel scattering calculations for three sets of scattering lengths compared with measured rates (red/gray squares). Dotted lines are energy-resolved rates and solid lines are thermally averaged rates. The lowest rates are obtained for $a_T = a_S = R_4$ (light red/gray) and the highest for $a_T = -a_S = R_4$ (blue/dark gray) within the three sets shown over a broad temperature range.

waves l ,

$$K_{\text{el}}^i(E) = \frac{\pi\hbar}{\mu k_i} \sum_{l=0}^{\infty} (2l+1) |1 - S_{ii}^l(E)|^2, \quad (5)$$

$$K_{\text{in}}^i(E) = \frac{\pi\hbar}{\mu k_i} \sum_{l=0}^{\infty} (2l+1) (1 - |S_{ii}^l(E)|^2),$$

and state-to-state inelastic $K_{\text{in}}^{ij}(E)$ rate constants for the transition between i -th and j -th channels from the off-diagonal elements of the S matrix summed over partial waves l ,

$$K_{\text{in}}^{ij}(E) = \frac{\pi\hbar}{\mu k_i} \sum_{l=0}^{\infty} (2l+1) |S_{ij}^l(E)|^2. \quad (6)$$

Here $k_i = \sqrt{2\mu(E - E_i^\infty)}/\hbar$ is the i -th channel wave vector with E the collision energy and E_i^∞ the i -th threshold energy.

The spin-exchange rates between different states of the Yb^+ ion colliding with Li atoms are calculated as a sum over all possible state-to-state transitions obtained with Eq. (6). The exemplary decompositions of the total spin-exchange rates for the $|1,0\rangle$ and $|1,-1\rangle$ states of the $^{171}\text{Yb}^+$ ion colliding with $|3/2, 3/2\rangle$ state ^6Li atoms are presented in Fig. 8. The opening of relevant spin channels at an energy of 0.1 mK can be seen. These calculations also confirm that the $\Delta m_F = +2$ transitions are negligible at our experimental conditions.

Spin-exchange rates depend on the difference between

singlet and triplet scattering phases [38]. Results for the $^{171}\text{Yb}^+$ ion are presented in Fig. 9. It can be seen that even in the mK temperature regime the spin-exchange rates still depend strongly on the difference between assumed singlet (a_S) and triplet (a_T) scattering lengths [43, 44]. To reproduce the large spin-exchange rates measured, the difference between the scattering lengths has to be close to the one that maximizes the scattering phase difference, that is $|a_T - a_S| = 2R_4$, where $R_4 = 1319$ bohr for $\text{Yb}^+/^6\text{Li}$. Similar results are found for the $^{174}\text{Yb}^+$ ion. If we take into account that part of the measured rates may be due to spin-nonconserving transitions, the difference between singlet and triplet scattering lengths is still restricted to a large value $R_4 < |a_T - a_S| < 3R_4$, assuming the largest measured values of the spin-nonconserving rates. The large difference between singlet and triplet scattering length also has another meaningful consequence, namely that broad magnetic Feshbach resonances can be expected when the s -wave regime of collisions is reached [38, 40].

B. Magnetically tunable Feshbach resonances

To assess the prospects for the observation and application of magnetically tunable Feshbach resonances in cold $\text{Yb}^+/^6\text{Li}$ collisions, we calculate thermally averaged rates for elastic and inelastic collisions as a function of a magnetic field between 0 and 1000 Gauss. We consider several possible entrance channels of the $^{174}\text{Yb}^+/^6\text{Li}$ and $^{171}\text{Yb}^+/^6\text{Li}$ systems at collision energies of $E_{\text{col}}/k_B = 100$ nK, $10 \mu\text{K}$ and 1 mK. We assume the difference between the singlet and triplet scattering lengths to be close to the one that maximizes the scattering phase difference, that is $|a_T - a_S| = 2R_4$, to reproduce the observed large rates for spin-exchange collisions.

An example result for $^{174}\text{Yb}^+/^6\text{Li}$ is presented in Fig. 10. Based on our detailed analysis, we can draw some general conclusions. First of all, for the assumed difference of the singlet and triplet scattering lengths, several measurable resonances are expected for experimentally accessible magnetic fields below 500 G for most values of M_{tot} at the energetically lowest channels. For higher energy channels, the resonances start to be less pronounced due to possible spin-exchange losses. At the same time, however, magnetic resonances can be used to control spin-exchange rates to a large extent. For spin-polarized collisions or very energetic channels no Feshbach resonances are expected. The temperature-dependence visible in Fig. 10 is typical for all combinations investigated. For collision energies deep in the quantum regime $E_{\text{col}} = k_B \cdot 100$ nK the Feshbach resonances are very pronounced. For $E_{\text{col}} = k_B \cdot 1$ mK they are not present because of the contribution of many partial waves and thermal averaging. Finally, for $E_{\text{col}} = k_B \cdot 10 \mu\text{K}$, which should be in reach in the present system [35], elastic collisions are dominated by contributions from s - and p -waves only, and broad and measurable res-

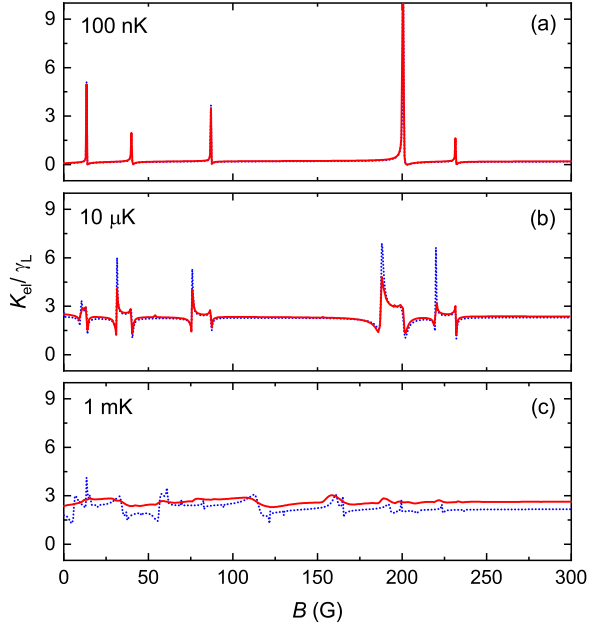


FIG. 10. Elastic scattering rates for $^{174}\text{Yb}^+/\text{}^6\text{Li}$ versus magnetic field for the lowest channel with $M_F = m_{f,\text{Yb}^+} + m_{f,\text{Li}} = 0$ at (a) $E_{\text{col}}/k_B = 100\text{ nK}$, (b) $10\text{ }\mu\text{K}$, and (c) 1 mK . The singlet scattering length is set to $a_S = -R_4$ and the triplet scattering length to $a_T = R_4$. Blue dotted lines are energy-resolved rates and red solid lines are thermally averaged rates.

onances can be expected.

C. Spin-relaxation

The spin-nonconserving relaxation is governed by the effective Hamiltonian describing dipolar-like interaction between the electronic spins of the Yb^+ ion, \hat{s}_{Yb^+} , and the Li atom, \hat{s}_{Li} [37, 55]

$$\hat{H}_{\text{dip}} = \left(-\frac{\alpha^2}{R^3} + \lambda_{\text{SO}}(R) \right) [3\hat{s}_{\text{Yb}^+}^z \hat{s}_{\text{Li}}^z - \hat{s}_{\text{Yb}^+} \cdot \hat{s}_{\text{Li}}], \quad (7)$$

where α is the fine-structure constant. The first term $-\frac{\alpha^2}{R^3}$ describes the contribution due to the direct magnetic dipole-dipole interaction. The second and dominating term $\lambda_{\text{SO}}(R)$ describes the effective dipole-dipole interaction in the second order of perturbation theory due to the first-order spin-orbit couplings between the $a^3\Sigma^+$ triplet electronic ground state and $^3\Pi$ electronic excited states. This interaction was identified as the main source of spin-nonconserving relaxation in the Yb^+/Rb system [14, 37].

The spin-orbit coupling coefficient $\lambda_{\text{SO}}(R)$ can be calculated from the energy difference between the $a0^-$ and $a1$ relativistic electronic states [37] or using second-order perturbation theory with non-relativistic electronic states and matrix elements of the spin-orbit coupling Hamiltonian between them [55]. Using the latter ap-

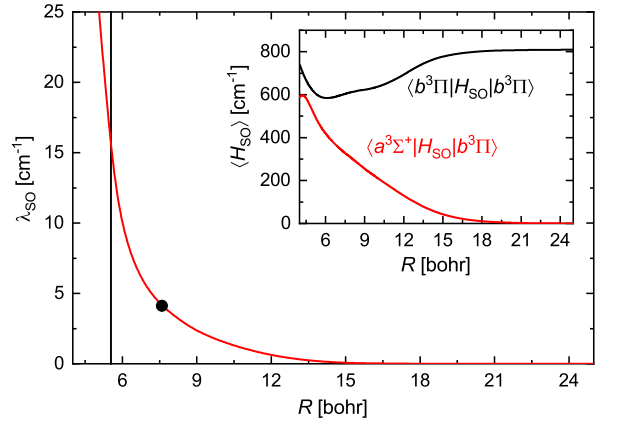


FIG. 11. Second-order spin-orbit coupling coefficient $\lambda_{\text{SO}}(R)$ for the Yb^+/Li system (red/gray line) as a function of the atom-ion distance. The point and vertical line indicate the value for the equilibrium distance and the position of the classical turning point of the $a^3\Sigma^+$ electronic state, respectively. The inset shows the matrix elements of the spin-orbit coupling for the $a^3\Sigma^+$ (red/gray) and $b^3\Pi$ (black) electronic states of the Yb^+/Li system.

proach, we calculate the spin-orbit coupling coefficient given by

$$\lambda_{\text{SO}}(R) = \frac{2}{3} \frac{|\langle a^3\Sigma^+ | H_{\text{SO}} | b^3\Pi \rangle|^2}{V_{b^3\Pi}(R) - V_{a^3\Sigma^+}(R)}, \quad (8)$$

where $\langle a^3\Sigma^+ | H_{\text{SO}} | b^3\Pi \rangle$ is the matrix element of the spin-orbit coupling between the $a^3\Sigma^+$ and $b^3\Pi$ electronic states. $V_{b^3\Pi}(R)$ and $V_{a^3\Sigma^+}(R)$ are potential energy curves of the $a^3\Sigma^+$ and $b^3\Pi$ electronic states which we calculated accurately in Ref. [40]. In Eq. (8) we neglected terms originating from the coupling between the $a^3\Sigma^+$ triplet ground state and higher $^3\Pi$ states because these terms should be much smaller due to a smaller spin-orbit coupling in the numerator and a larger energy difference in the denominator. The matrix elements of the spin-orbit coupling Hamiltonian, H_{SO} , are evaluated using wave functions calculated using *ab initio* electronic structure methods from Ref. [56].

The matrix elements of the spin-orbit coupling for the $a^3\Sigma^+$ and $b^3\Pi$ electronic states are presented in the inset of Fig. 11. The matrix element of the spin-orbit coupling for the $b^3\Pi$ electronic state $\langle b^3\Pi | H_{\text{SO}} | b^3\Pi \rangle$ asymptotically reaches the value which reproduces the experimental spin-orbit splitting of the 3P state of the Yb atom [57]. This confirms the quality of our calculations. The matrix element of the spin-orbit coupling between the $a^3\Sigma^+$ and $b^3\Pi$ electronic states $\langle a^3\Sigma^+ | H_{\text{SO}} | b^3\Pi \rangle$ decreases exponentially with the atom-ion distance as expected but at the equilibrium distance of the $a^3\Sigma^+$ electronic state it still has a significant value of 323 cm^{-1} .

The calculated second-order spin-orbit coupling coefficient $\lambda_{\text{SO}}(R)$ is presented in Fig. 11. It decreases exponentially with the atom-ion distance but at the equi-

librium distance and classical turning point of the $a^3\Sigma^+$ electronic state it has a value of 4.1 cm^{-1} and 14.2 cm^{-1} , respectively. These values are an order of magnitude smaller than for the Yb^+/Rb system [37, 58] and an order of magnitude larger than for neutral alkali-metal atoms [55]. The larger second-order spin-orbit coupling coefficient for the Yb^+/Rb system is due to the small energy difference and crossing between the $a^3\Sigma^+$ and $b^3\Pi$ electronic states and a contribution from the Rb atom to the spin-orbit interaction which is smaller for the very light Li atom. The spin-orbit coupling for neutral alkali-metal atoms is smaller because relativistic effects are smaller for alkali-metal atoms as compared to the heavy Yb^+ ion.

V. CONCLUSIONS

We have measured the spin dynamics of single trapped Yb^+ ions immersed in a cold cloud of spin-polarized ^6Li atoms. This combination is of significant interest as its large mass ratio may allow it to reach the quantum regime in Paul traps [31, 35]. We have observed very fast spin-exchange that occurs within a few Langevin collisions. Spin-relaxation rates are found to be a factor $\geq 13(7)$ smaller than spin-exchange rates in $^{174}\text{Yb}^+$. Spin impurity atoms in the atomic cloud may lead to apparent spin-relaxation, such that we interpret the observed relaxation rate as an upper limit. The observed ratio between spin-allowed and spin-nonconserving collisions is higher than those observed in Yb^+/Rb [14], where a ratio of $0.56(8)$ was measured for Rb atoms in the

stretched $|F=2, m_F=2\rangle$ state. For Sr^+/Rb [19], both spin-exchange and spin-relaxation rates for Rb atoms prepared in the $|F=1, m_F=-1\rangle$ state are lower than the rates observed in this work and have a lower ratio of $5.2(8)$. For $^{171}\text{Yb}^+$, we have measured the decay channels of all spin states within the ground state hyperfine manifold and observe both spin-exchange and spin-relaxation processes. We have compared our measured rates to predictions from *ab initio* electronic structure and quantum scattering calculations and conclude that a large difference between singlet and triplet scattering lengths is responsible for the observed large spin-exchange rates, whereas small second-order spin-orbit coupling results in small spin-relaxation rates. These findings suggest good prospects for the observation of Feshbach resonances in the Yb^+/Li system.

ACKNOWLEDGEMENTS

This work was supported by the European Union via the European Research Council (Starting Grant 337638) and the Netherlands Organization for Scientific Research (Vidi Grant 680-47-538 and Start-up grant 740.018.008) (R.G.). M.T. was supported by the National Science Centre Poland (Opus Grant 2016/23/B/ST4/03231) and PL-Grid Infrastructure.

REFERENCES

-
- [1] W. W. Smith, O. P. Makarov, and J. Lin, *J. Mod. Opt.* **52**, 2253 (2005).
 - [2] A. T. Grier, M. Cetina, F. Oručević, and V. Vuletić, *Phys. Rev. Lett.* **102**, 223201 (2009).
 - [3] C. Zipkes, S. Paltzer, C. Sias, and M. Köhl, *Nature* **464**, 388 (2010).
 - [4] S. Schmid, A. Härter, and J. H. Denschlag, *Phys. Rev. Lett.* **105**, 133202 (2010).
 - [5] C. Zipkes, S. Palzer, L. Ratschbacher, C. Sias, and M. Köhl, *Phys. Rev. Lett.* **105**, 133201 (2010).
 - [6] F. H. J. Hall, M. Aymar, N. Bouloufa-Maafa, O. Dulieu, and S. Willitsch, *Phys. Rev. Lett.* **107**, 243202 (2011).
 - [7] F. H. J. Hall and S. Willitsch, *Phys. Rev. Lett.* **109**, 233202 (2012).
 - [8] W. G. Rellergert, S. T. Sullivan, S. Kotochigova, A. Petrov, K. Chen, S. J. Schowalter, and E. R. Hudson, *Phys. Rev. Lett.* **107**, 243201 (2011).
 - [9] S. T. Sullivan, W. G. Rellergert, S. Kotochigova, and E. R. Hudson, *Phys. Rev. Lett.* **109**, 223002 (2012).
 - [10] L. Ratschbacher, C. Zipkes, C. Sias, and M. Köhl, *Nat. Phys.* **8**, 649652 (2012).
 - [11] K. Ravi, S. Lee, A. Sharma, G. Werth, and S. A. Rangwala, *Nat. Commun.* **3**, 1126 (2012).
 - [12] A. Härter and J. H. Denschlag, *Contemp. Phys.* **55**, 33 (2014).
 - [13] F. H. Hall, P. Eberle, G. Hegi, M. Raoult, M. Aymar, O. Dulieu, and S. Willitsch, *Mol. Phys.* **111**, 2020 (2013).
 - [14] L. Ratschbacher, C. Sias, L. Carcagni, J. M. Silver, C. Zipkes, and M. Köhl, *Phys. Rev. Lett.* **110**, 160402 (2013).
 - [15] S. Haze, R. Saito, M. Fujinaga, and T. Mukaiyama, *Phys. Rev. A* **91**, 032709 (2015).
 - [16] Z. Meir, T. Sikorsky, R. Ben-shlomi, N. Akerman, Y. Dallel, and R. Ozeri, *Phys. Rev. Lett.* **117**, 243401 (2016).
 - [17] R. Côté, *Adv. in AMO Phys.* **65**, 67 (2016).
 - [18] M. Tomza, K. Jachymski, R. Gerritsma, A. Negretti, T. Calarco, Z. Idziaszek, and P. S. Julienne, ArXiv e-prints (2017), [arXiv:1708.07832](https://arxiv.org/abs/1708.07832) [physics.atom-ph].
 - [19] T. Sikorsky, Z. Meir, R. Ben-shlomi, N. Akerman, and R. Ozeri, *Nature Communications* **9**, 920 (2018).
 - [20] S. Haze, M. Sasakawa, R. Saito, R. Nakai, and T. Mukaiyama, *Phys. Rev. Lett.* **120**, 043401 (2018).
 - [21] K. S. Kleinbach, F. Engel, T. Dieterle, R. Löw, T. Pfau, and F. Meinert, *Phys. Rev. Lett.* **120**, 193401 (2018).
 - [22] R. Côté and A. Dalgarno, *Phys. Rev. A* **62**, 012709 (2000).

- [23] M. Krych, W. Skomorowski, F. Pawłowski, R. Moszynski, and Z. Idziaszek, *Phys. Rev. A* **83**, 032723 (2011).
- [24] M. Krych and Z. Idziaszek, *Phys. Rev. A* **91**, 023430 (2015).
- [25] T. Secker, N. Ewald, J. Joger, H. Fürst, T. Feldker, and R. Gerritsma, *Phys. Rev. Lett.* **118**, 263201 (2017).
- [26] C. Kollath, M. Köhl, and T. Giamarchi, *Phys. Rev. A* **76**, 063602 (2007).
- [27] H. Doerk, Z. Idziaszek, and T. Calarco, *Phys. Rev. A* **81**, 012708 (2010).
- [28] T. Secker, R. Gerritsma, A. W. Glaetzle, and A. Negretti, *Phys. Rev. A* **94**, 013420 (2016).
- [29] U. Bissbort, D. Cocks, A. Negretti, Z. Idziaszek, T. Calarco, F. Schmidt-Kaler, W. Hofstetter, and R. Gerritsma, *Phys. Rev. Lett.* **111**, 080501 (2013).
- [30] L. H. Nguyen, A. Kalev, M. Barrett, and B.-G. Englert, *Phys. Rev. A* **85**, 052718 (2012).
- [31] M. Cetina, A. T. Grier, and V. Vuletić, *Phys. Rev. Lett.* **109**, 253201 (2012).
- [32] K. Chen, S. T. Sullivan, and E. R. Hudson, *Phys. Rev. Lett.* **112**, 143009 (2014).
- [33] B. Höltkemeier, P. Weckesser, H. López-Carrera, and M. Weidemüller, *Phys. Rev. Lett.* **116**, 233003 (2016).
- [34] I. Rouse and S. Willitsch, *Phys. Rev. Lett.* **118**, 143401 (2017).
- [35] H. A. Fürst, N. V. Ewald, T. Secker, J. Joger, T. Feldker, and R. Gerritsma, ArXiv e-prints (2018), [arXiv:1804.04486](https://arxiv.org/abs/1804.04486) [physics.atom-ph].
- [36] O. P. Makarov, R. Côté, H. Michels, and W. W. Smith, *Phys. Rev. A* **67**, 042705 (2003).
- [37] T. V. Tscherbul, P. Brumer, and A. A. Buchachenko, *Phys. Rev. Lett.* **117**, 143201 (2016).
- [38] C. Chin, R. Grimm, P. S. Julienne, and E. Tiesinga, *Rev. Mod. Phys.* **82**, 1225 (2010).
- [39] Z. Idziaszek, A. Simoni, T. Calarco, and P. S. Julienne, *New J. Phys.* **13**, 083005 (2011).
- [40] M. Tomza, C. P. Koch, and R. Moszynski, *Phys. Rev. A* **91**, 042706 (2015).
- [41] M. Gacesa and R. Côté, *Phys. Rev. A* **95**, 062704 (2017).
- [42] I. Bloch, J. Dalibard, and S. Nascimbène, *Nat. Phys.* **8**, 267 (2012).
- [43] T. Sikorsky, M. Morita, Z. Meir, A. A. Buchachenko, R. Ben-shlomi, N. Akerman, E. Narevicius, T. V. Tscherbul, and R. Ozeri, ArXiv e-prints (2018), [arXiv:1806.05150](https://arxiv.org/abs/1806.05150) [physics.atom-ph].
- [44] R. Côté and I. Simbotin, ArXiv e-prints (2018), [arXiv:1806.06162](https://arxiv.org/abs/1806.06162) [physics.atom-ph].
- [45] J. Joger, H. Fürst, N. Ewald, T. Feldker, M. Tomza, and R. Gerritsma, *Phys. Rev. A* **96**, 030703(R) (2017).
- [46] F. Mintert and C. Wunderlich, *Phys. Rev. Lett.* **87**, 257904 (2001).
- [47] C. Ospelkaus, U. Warring, Y. Colombe, K. R. Brown, J. M. Amini, D. Leibfried, and D. J. Wineland, *Nature* **476**, 181 (2011).
- [48] P. Taylor, M. Roberts, S. V. Gateva-Kostova, R. B. M. Clarke, G. P. Barwood, W. R. C. Rowley, and P. Gill, *Phys. Rev. A* **56**, 2699 (1997).
- [49] E. Biémont, J.-F. Dutrieux, I. Martin, and P. Quinet, *Journal of Physics B: Atomic, Molecular and Optical Physics* **31**, 3321 (1998).
- [50] T. Feldker, H. Fürst, N. V. Ewald, J. Joger, and R. Gerritsma, *Phys. Rev. A* **97**, 032511 (2018).
- [51] S. Olmschenk, K. C. Younge, D. L. Moehring, D. N. Matsukevich, P. Maunz, and C. Monroe, *Phys. Rev. A* **76**, 052314 (2007).
- [52] M. Houbiers, H. T. C. Stoof, W. I. McAlexander, and R. G. Hulet, *Phys. Rev. A* **57**, R1497 (1998).
- [53] M. Tomza, R. González-Férez, C. P. Koch, and R. Moszynski, *Phys. Rev. Lett.* **112**, 113201 (2014).
- [54] B. R. Johnson, *J. Chem. Phys.* **69**, 4678 (1978).
- [55] F. H. Mies, C. J. Williams, P. S. Julienne, and M. Krauss, *J. Res. Natl. Inst. Stand. Technol.* **101**, 521 (1996).
- [56] M. Tomza, M. H. Goerz, M. Musiał, R. Moszynski, and C. P. Koch, *Phys. Rev. A* **86**, 043424 (2012).
- [57] NIST Atomic Spectra Database <http://physics.nist.gov/PhysRefData/ASD>.
- [58] E. R. Sayfutyarova, A. A. Buchachenko, S. A. Yakovleva, and A. K. Belyaev, *Phys. Rev. A* **87**, 052717 (2013).